A&A 671, A86 (2023)
https://doi.org/10.1051/0004-6361/202245250

Astronomy & Astrophysics

Study of oxygen-rich post-AGB stars in the Milky Way as a means to explain the production of silicates among evolved stars

F. Dell'Agli[1], S. Tosi[1,2], D. Kamath[1,3,4], P. Ventura[1,5], H. Van Winckel[6], E. Marini[1], and T. Marchetti[7]

[1] INAF, Observatory of Rome, Via Frascati 33, 00077 Monte Porzio Catone, RM, Italy
e-mail: flavia.dellagli@inaf.it
[2] Dipartimento di Matematica e Fisica, Università degli Studi Roma Tre, Via della Vasca Navale 84, 00100 Roma, Italy
[3] School of Mathematical and Physical Sciences, Macquarie University, Sydney, NSW, Australia
[4] Astronomy, Astrophysics and Astrophotonics Research Centre, Macquarie University, Sydney, NSW, Australia
[5] Istituto Nazionale di Fisica Nucleare, Section of Perugia, Via A. Pascoli snc, 06123 Perugia, Italy
[6] Institute of Astronomy, KU Leuven, Celestijnenlaan 200D Bus 2401, 3001 Leuven, Belgium
[7] European Southern Observatory, Karl-Schwarzschild-Strasse 2, 85748 Garching bei München, Germany

Received 19 October 2022 / Accepted 21 November 2022

ABSTRACT

Context. The study of post-asymptotic giant branch (post-AGB) stars is a valuable tool in improving our understanding of poorly known aspects of the evolution of the stars throughout the asymptotic giant branch (AGB). This can be done thanks to the availability of more accurate determinations of their surface chemical composition and the peculiar shape of their spectral energy distribution (SED): the emission from the central star can be easily disentangled from the contribution from the dusty shell, which can then be characterized.
Aims. The goal of the present study is to reconstruct the dust formation process and, more generally, the late phases of evolution for oxygen-rich stars across the AGB phase. This is performed by studying oxygen-rich, post-AGB stars and analyzing them in terms of their luminosity, effective temperature, and infrared excess.
Methods. We studied sources classified as single, oxygen-rich, post-AGB stars in the Galaxy that exhibit a double-peaked (shell-type) SED. We used results from stellar evolution modeling, combined with dust formation and radiative transfer modeling, to reconstruct late AGB phases and the initial contraction to the post-AGB phase. We also determined the mass-loss and dust-formation rates for stars of different masses and chemical compositions.
Results. The analysis of the IR excess of the post-AGB, oxygen-rich stars examined in this study outlines an interesting complexity with regard to the correlation between the dust in the surroundings of the stars, the evolutionary status, and the progenitor's mass. The sources descending from massive AGBs (>3 $M_{\odot}$, depending on metallicity) are generally characterized by higher infrared excess than the lower mass counterparts, owing to the more intense dust formation taking place during the final AGB phases. From the determination of the location of the dusty regions, we can deduce that the expanding velocities of the outflow change significantly from star to star. We also discuss the possibility that radiation pressure is not able of accelerating the wind in the faintest objects.

Key words. stars: AGB and post-AGB – galaxies: stellar content – dust, extinction

1. Introduction

Stars evolving through the asymptotic giant branch (AGB) are generally regarded as one of the most important contributors to the reprocessed gas of the interstellar medium. The knowledge of the AGB gas yields is crucial in reconstructing the chemical evolution of the Milky Way (Romano et al. 2010; Kobayashi et al. 2020) and the chemical patterns observed in star-forming galaxies in the Local Group (Vincenzo et al. 2016). Furthermore, the winds of AGB stars are a favourable site for the production of dust, which is the reason dust from AGB stars accounts for a significant fraction of the overall dust budget in mature galaxies of the present day (Zhukovska et al. 2008; Sloan et al. 2009). The dust manufactured by AGB stars is a fundamental ingredient for studying the dust content of the Milky Way (Ginolfi et al. 2018) and to model the evolution of the dust content in local and high-redshift galaxies (Nanni et al. 2020).

Overall, AGB stars are extremely complex objects. The convective envelope, that can be safely described under ideal gas conditions, coexists with the degenerate core, composed of carbon and oxygen (Busso et al. 1999; Herwig 2005; Karakas & Lattanzio 2014) or oxygen and neon for $M \geq 7\,M_{\odot}$ (García-Berro et al. 1997). Despite significant steps forward that have been achieved in recent decades by a number of research teams (Cristallo et al. 2015; Karakas & Lugaro 2016; Karakas et al. 2018, 2022; Cinquegrana & Karakas 2022; Ventura et al. 2018, 2020, 2021), the description of the AGB phase is still severely limited by the dearth of knowledge in terms of the physical mechanisms, mainly convection and mass loss, that play a relevant role on the evolution of AGB stars (Ventura & D'Antona 2005a,b).

A notable contribution towards achieving a deeper understanding of the evolution of AGB stars has been provided by the study of post-AGB stars. Indeed, the surface chemical composition of post-AGB stars is a key indicator of the relative importance of the two mechanisms in altering the surface chemistry of the stars evolving through the AGB phase; namely hot bottom burning (HBB, Blöcker & Schöenberner 1991) and third dredge-up (TDU, Iben 1974). Furthermore, owing to the warmer photospheres (A-K spectral types) of post-AGB stars, their spectra are dominated by atomic transitions, providing a unique possibility for deriving accurate photospheric chemical abundances of a wide range of elements (e.g., CNO, alpha and Fe-peak elements, and *s*-process elements; see Kamath 2020; Kamath & Van Winckel 2022 and references therein). On the other hand, obtaining surface abundances for a wide range

of elements using AGB star spectra is challenging since they have complex and dynamical atmospheres and their spectra are severely affected by molecular bands (García-Hernández et al. 2009).

Typical examples of studies where observations of post-AGB have been used to understand AGB nucleosynthesis include De Smedt et al. (2012) and Kamath et al. (2017). More recently, Kamath et al. (2022) capitalized on the reliable distance estimates derived from *Gaia* EDR3/DR3 to study 31 single Galactic post-AGB stars (13 oxygen-rich with no *s*-process enrichment and 19 carbon-rich and *s*-process objects) with well-studied surface abundances and derived their luminosites – a parameter that is critical in identifying the initial mass of the stars. A thorough derivation of the progenitors and of the evolutionary history of these stars was presented in Kamath et al. (2023).

A further advantage of the study of post-AGB stars is that the spectral energy distribution (SED) exhibits a typical double-peak shape referred to as a "shell-type" SED (van Winckel 2003), which allows us to disentangle the emission from the central object and the infrared excess due to the presence of dust in the surrounding of the star. This is extremely important with regard to testing the dust formation modeling in the winds of evolved stars, as recently implemented into the description of the AGB phase by various research teams (Ventura et al. 2012, 2014; Nanni et al. 2013, 2014), then applied to interpret infrared (IR) observations and characterizations of AGB stars of the Magellanic Clouds (MC; Dell'Agli et al. 2014a,b, 2015a,b; Nanni et al. 2016, 2019) and Local Group galaxies (Dell'Agli et al. 2016, 2018, 2019, 2021).

The first application of this analysis was published by Tosi et al. (2022, hereafter Paper I), using the study of single post-AGB stars to draw information regarding the previous AGB phase. This work was focused on 13 likely single sources in the MC, classified as a shell-type by Kamath et al. (2014, 2015), who provided the effective temperatures and metallicities, along with a detailed reconstruction of the SED. The comparison with results from AGB evolution and dust formation modeling allowed us to characterize the individual sources presented in Kamath et al. (2014, 2015) in terms of mass and formation epoch of the progenitors and to draw interesting conclusions on the mass-loss rates experienced by stars during the final AGB phases and on the dynamics of the outflow.

In the present work, we apply the methodology proposed in Paper I to study the 13 oxygen-rich objects in the sample by Kamath et al. (2022). This will allow for a more exhaustive investigation of the evolutionary properties of the stars that do not become carbon stars with respect to Paper I. Indeed, the five Large Magellanic Clouds (LMC) oxygen-rich stars without any *s*-process enrichment investigated in Paper I were substantially homogeneous in terms of luminosity and optical depth. The interpretation given in Paper I was based on the assumption that they are the progeny of low-mass stars that experienced none or only a few TDU episodes, thereby preventing any significant *s*-process enrichment and, thus, the possibility to reach the carbon star stage. On the other hand, the Galactic non *s*-process enriched sources presented in Kamath et al. (2022) exhibit a diversity ranging from those with large IR excesses to those without significant circumstellar dust. Moreover, compared to the LMC sample presented in Paper I, the luminosity range of the target stars in this study are much more extended (see Kamath et al. 2022).

The current paper is structured as follows. We present the methodology we followed to characterize the individual sources in Sect. 2. The classification of the stars in the sample and of the dust in their surroundings is given in Sect. 3. In Sect. 4, we discuss the dynamical properties of the outflow and the differences found with respect to carbon stars. Finally, our conclusions are given in Sect. 5.

2. Methodology for characterizing the individual sources

We first selected 13 oxygen-rich post-AGB stars, drawn from Kamath et al. (2022). We applied the same approach used in Paper I to discuss and characterize the post-AGB stars in the MC. This methodology can be summarized as three basic steps:

First, the SED of each source was constructed on the basis of the photometric data collected by Kamath et al. (2022) and considering the Infrared Space Observatory (ISO) spectrum (Sloan et al. 2003), when available. The SED fitting was achieved by means of the radiative transfer code DUSTY (Nenkova et al. 1999), starting from the effective temperatures given in Kamath et al. (2022). DUSTY is used in the spherical modality, with the gas density declining with distance as $\propto r^{-2}$. The determination of the main physical parameters is eased by the peculiar morphology of the SED of these objects. Indeed, this procedure leads to the determination of the optical depth at $\lambda = 10\,\mu$m, τ_{10} (mainly related to the height of the peak of the SED in the mid-IR) and of $T_{\rm d}$, the dust temperature connected to the depth of the minimum of the SED separating the dust IR excess to the emission from the central object. We note that $T_{\rm d}$ is tightly correlated to the distance of the inner border of the dusty zone, $R_{\rm in}$, from the centre of the star. Typical uncertainties associated with these estimates are $\sim$10–15% in τ_{10} and $\sim$20 K for $T_{\rm d}$. The distribution of the IR data provides indication on the presence of a pure amorphous silicate dust composition (optical constants from Draine & Lee 1984, DL hereafter) or whether a percentage of crystalline silicates (optical constants from Jaeger et al. 1994) is present.

Next, to identify the progenitor's mass, we used the evolutionary tracks of stars of different mass and metallicities calculated by means of the ATON code for stellar evolution (Ventura et al. 1998), which is thoroughly discussed in Kamath et al. (2023). To this aim, we compared the position of the tracks on the HR diagram with the effective temperatures and the luminosities of the individual sources. We used the metallicity and the effective temperatures given in Kamath et al. (2022). Regarding the luminosities, we note that unlike Paper I (which focused on MC sources), here we adopted a distance for each object within the range given by Bailer-Jones et al. (2021). The uncertainties on the distances reflect into a range of possible luminosities to be considered, as found by Kamath et al. (2022; see their Table 1). The choice of the distance, still within the limits mentioned above, is done by looking for consistency between the whole observational framework of the individual stars (surface chemical abundances and dust mineralogy) and the results from stellar evolution and dust formation modeling. We note that the accuracy with which the distance is known sets a natural discrimination between the stars labeled as Q1 (RUWE[1] < 1.4) in Kamath et al. (2022). We use this accuracy as the basis for most

[1] RUWE refers to the renormalized unit weight error, which is defined as the magnitude and colour-renormalized square root of the reduced chi-squared statistic to the *Gaia* astrometric fit (Lindegren et al. 2021). A value of RUWE < 1.4 is often employed to select stars with accurate parallaxes and proper motions, while larger values could be a sign of binarity and, in general, of a poor astrometric fit (e.g., Belokurov et al. 2020; Penoyre et al. 2020).

of our interpretation; those flagged as Q2 (RUWE $\gtrsim 1.4$) are the ones with distances that are much more uncertain, which is then reflected in their poor determinations for the luminosities.

Finally, to connect the properties of the dust responsible for the IR excess observed presently with the dust production process during the previous AGB and early post-AGB phases, we modeled dust formation at the tip of the AGB phase (by which we mean the stage when the contraction to the post-AGB phase begins) and during some evolutionary stages distributed along the post-AGB phase. This step is aimed at finding a consistency between the results from stellar evolution and dust formation modeling with the observations, as well as to understand when the dust currently observed was released (see Sect. 5 in Paper I for more details). The dust formation was modeled according to Ventura et al. (2012, 2014), following the schematization proposed by the Heidelberg group (Ferrarotti & Gail 2006). The input for describing dust formation (i.e., mass, effective temperature, mass-loss rate, and surface chemical composition of the star) were taken from the results of the stellar evolution modeling. Because we are studying oxygen-rich stars only, the dust species considered are silicates (both in amorphous and crystalline form) and alumina dust (Ferrarotti & Gail 2006).

3. Dust properties of oxygen-rich Galactic post-AGB stars

The fit of the SED of the different sources considered here is shown in Figs. 1 and 2. A summary of the results obtained is reported in Table 1, which also gives the metallicity, effective temperature, and luminosity range for each source, as derived by Kamath et al. (2022). The IDs in Col. 2 are the same as in Kamath et al. (2022, 2023). The distribution of the star in the HR diagram is shown in Fig. 3, where the evolutionary tracks of some model stars used later in this section to characterize the sample sources are also indicated.

Similarly to Paper I, to discuss the results, we analyzed the trend of τ_{10} as a function of the luminosity and of $R_{\rm in}$, shown, respectively, in the left and right panels of Fig. 4. In the remainder of this section, we consider groups of stars sharing similar dust properties or progenitor mass, and we discuss them individually.

3.1. The oxygen-rich and carbon-star interface

The stars ID 24 and ID 30 were determined by Kamath et al. (2023) to be low-mass stars that have lost their envelopes after only a few TDU events and did not turn into carbon stars (see Fig. 2 in Kamath et al. 2023). In line with this interpretation, we see in the left panel of Fig. 4 that the two sources populate the same region as the four LMC oxygen-rich stars discussed in Paper I – for this reason, we refer to them as "MC-type" stars. In Paper I, they were also identified as low-mass stars that had not reached the C-star stage.

Among this group, ID 30 is the source with the highest τ_{10} ($\tau_{10} = 0.09$, while the average is typically $\tau_{10} \sim 0.03$), which is the effect of the higher luminosity and the higher mass-loss rate experienced at the end of the AGB phase. The luminosity range of ID 30 given in Kamath et al. (2022), namely, 5955−7545 $L_{\odot}$, is consistent with the interpretation given in Kamath et al. (2023) – but only when values close to the lower limit are considered (see Fig. 3 in Kamath et al. 2023).

To test whether a satisfactory agreement between the physical and dust parameters derived from the observations and from the SED fitting with the results from stellar evolution + dust formation modeling can be reached, we investigated ID 30 in detail. Because the metallicity of this star is higher than the other low-luminosity sources for which we propose a similar origin, all sharing a sub-solar chemical composition, we considered solar metalicity models that were specifically calculated for the present investigation.

The left panel of Fig. 5 shows the evolutionary track of a 1.1 $M_{\odot}$ model star of solar metallicity. We note that in agreement with Kamath et al. (2023), the value of the mass refers to the beginning of the core helium-burning phase, from which the evolutionary run is started. The post-AGB luminosity of this model star is ∼6700 $L_{\odot}$, which is within the luminosity range given by Kamath et al. (2022). Overall, this star experiences ten thermal pulses (TPs) and only two TDU events. As shown in the right panel of Fig. 5, the surface carbon increases up to [C/Fe] ∼ 0.2, consistently with the results given in Kamath et al. (2022), far below the threshold required to convert the star into a carbon star.

If we assume that the star lost 0.1 $M_{\odot}$ during the RGB, we derive a progenitor initial mass of 1.2 $M_{\odot}$, which corresponds to an age for ID 30 of ∼6 Gyr. The uncertainty associated with the derivation of the post-RGB mass of ID 30 given above is small. Indeed, if we consider masses of ∼1 $M_{\odot}$ we find post-AGB luminosities smaller than the lower limit for ID 30 given in Kamath et al. (2022). On the contrary, if we assume a higher mass, we find that the star experiences a higher number of TDU events than those shown in the right panel of Fig. 5 and eventually becomes a carbon star, with significant *s*-process enrichment.

Figure 5 shows that the 1.1 $M_{\odot}$ model star reaches a maximum size slightly in excess of 300 $R_{\odot}$ before starting the contraction process during the post-AGB phase. The mass-loss rate during the phase when the radius is largest, which we refer to as the tip of AGB (TAGB), is $\sim 2 \times 10^{-6}\, M_{\odot}\,{\rm yr}^{-1}$. This is about two times higher than the mass-loss rates of the low-luminosity oxygen-rich stars studied in Paper I, due to the higher luminosity and the larger metallicity.

In applying our dust formation modeling to the TAGB parameters we found for ID 30 ($L = 6700\, L_{\odot}$, $\dot{M} = 2 \times 10^{-6}\, M_{\odot}\,{\rm yr}^{-1}$, and effective temperature 3000 K) leads to a present-day optical depth of $\tau_{10} = 0.5$, significantly higher than the value derived from SED fitting. The possibility that the dust was released at the tip of the AGB can be also disregarded on the basis of dynamical arguments: indeed, the time required for the star to evolved from the TAGB to the current phase is found to be $\sim 10^4$ yr; this result, combined with the distance of the dusty region of ID 30 reported in Table 1, would imply velocities below 1 km s^{-1}, which is inconsistent with results from the observations and from dynamical modeling of radiation-driven stellar winds. On the other hand, if we assume that the dust responsible for the IR excess observed now was released when the effective temperature of the star reaches 3500 K, we find that $\tau_{10} \sim 0.1$, which is in agreement with the results shown in Fig. 1 and reported in Table 1. Considering the fact that the time between the phase when the effective temperature was 3500 K and the present epoch is found to be slightly below 1 Kyr, by assuming an expansion velocity of 10 km s^{-1}, we find that the dusty layer should currently be at a distance $\sim 4 \times 10^5\, R_{\odot}$ away from the central star. This is consistent with the analysis from the SED fitting (see the right panel of Fig. 4).

When compared to the five low-luminosity, oxygen-rich stars investigated in Paper I (shown as grey triangles in Fig. 4), it is clear that the dust has traveled further in the case of ID 30,

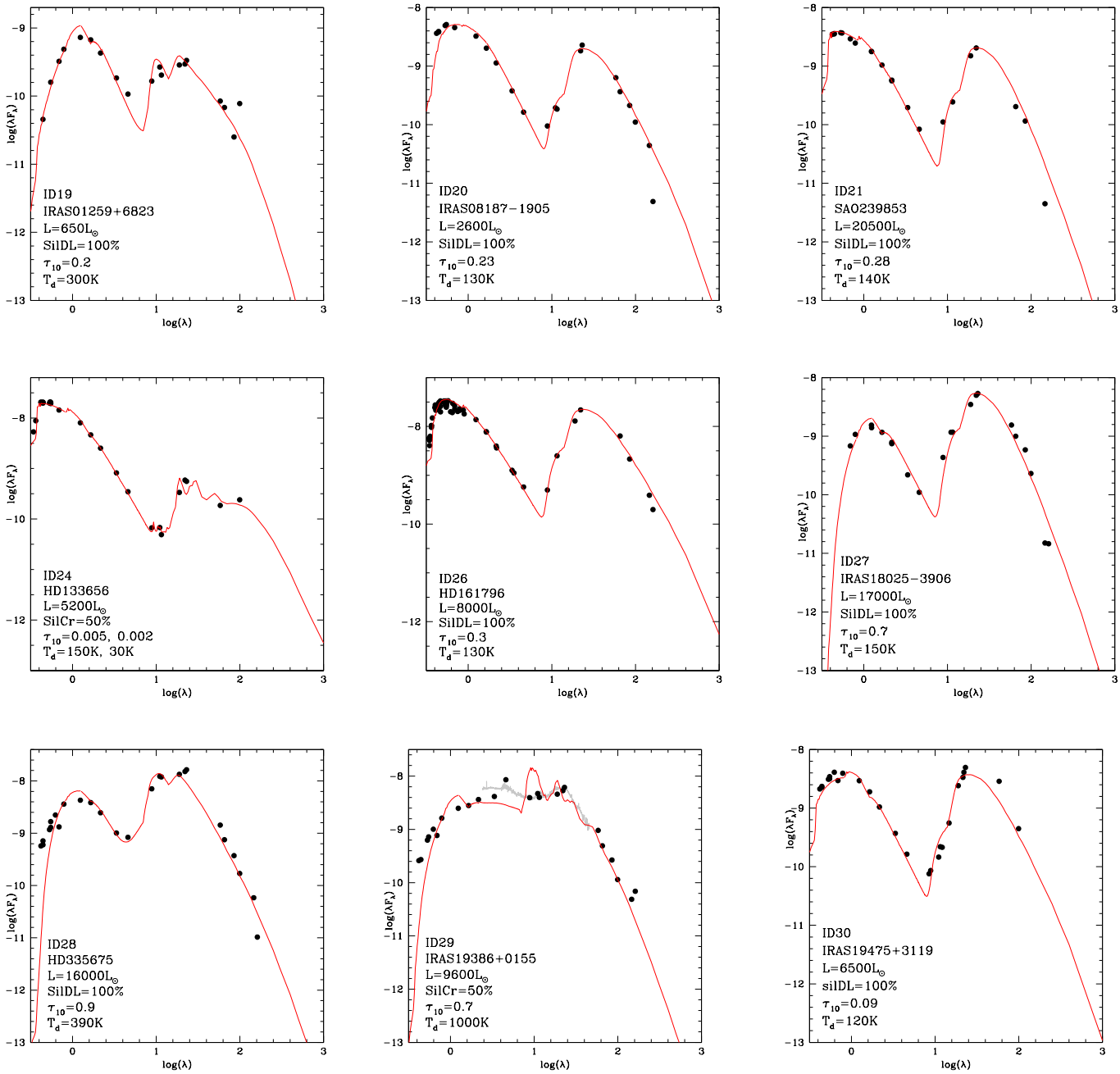

Fig. 1. Optical and IR data (black points) of oxygen-rich Galactic sources classified as post-AGB stars presented in Kamath et al. (2022), which we interpret as surrounded by silicate dust in the present investigation. The grey line line shows the ISO spectra from Sloan et al. (2003), when available. The red lines indicate the best-fit model obtained using the DUSTY code. The derived stellar and dust parameters from this study for each source are shown in the different panels.

reaching distances that are 3−10 times higher. We propose that this is related to the different optical depths, that leads to a more efficient dust formation process in the case of ID 30. In the stars discussed in Paper I the amount of dust manufactured was so small that the effects of the radiation pressure are reduced, thus, the velocities with which the outflow moved away from the star were of the order of a few km s^{-1}. In the case of ID 30, dust was produced in higher quantities, which favoured a stronger action from radiation pressure and which, in turn, was reflected in higher velocities of the outflow. Considering that ID 30 has higher luminosity and metallicity with respect to the LMC counterparts, this interpretation is consistent with the study from Goldman et al. (2017), who found that the expansion velocity of the outflow of oxygen-rich stars in the LMC and in the Galaxy are positively correlated with the metallicity and luminosity.

The source ID 24 is characterized by lower luminosity and metallicity than ID 30. The post-AGB luminosity of the star is reproduced by a 0.9 $M_{\odot}$ star of a metallicity $Z = 4 \times 10^{-3}$. By accounting for the fact that 0.1−0.2 $M_{\odot}$ were lost during the RGB phase, we deduce that this star formed 5−6 Gyr ago. The contraction time from the tip of the AGB to the current effective temperature $T_{\rm eff}$ = 8238 K is 2.5×10^4 yr, whereas the time from the stage when $T_{\rm eff}$ = 3500 K to its current status is 2500 Kyr.

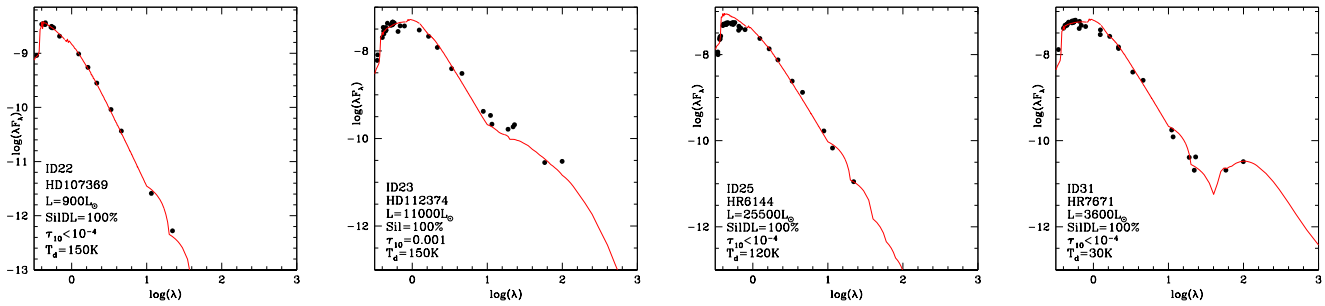

Fig. 2. Optical and IR data (black points) of oxygen-rich Galactic sources classified as post-AGB stars presented in Kamath et al. (2022), which we interpret as "dust-free" in the present investigation. This is due to the little if not null infrared excess that characterizes these sources.

Table 1. Physical and dust properties of the Galactic post-AGB stars targeted in this study.

Source	ID	[Fe/H]	$T_{\rm eff}$ [K]	$L/L_\odot$	$L/L_\odot^{\rm K22}$	τ_{10}	$T_{\rm d}$ [K]	$R_{\rm in}/R_\odot$	Flag
IRAS 01259+6823	19	−0.6 ± 0.1	5510	650	220–646	0.2	300	6.30×10^3	Q1
IRAS 08187–1905	20	−0.6 ± 0.1	5772	2600	2099–3286	0.23	130	1.55×10^5	Q2
SAO 239853	21	−0.8 ± 0.1	7452	20 500	13 080–48 520	0.28	140	3.80×10^5	Q2
HD 107369	22	−1.1 ± 0.1	7533	900	814–1010	$<10^{-4}$	150	–	Q1
HD 112374	23	−1.2 ± 0.1	6393	11 000	9961–11 882	$\leq10^{-3}$	150	6.45×10^4	Q1
HD 133656	24	−0.7 ± 0.1	8238	5200	4861–5690	0.005	150	2.00×10^5	Q1
HR 6144	25	−0.4 ± 0.1	6728	25 500	22 212–30 419	$<10^{-4}$	120	–	Q1
HD 161796	26	−0.3 ± 0.1	6139	8000	5209–6322	0.3	130	2.85×10^5	Q1
IRAS 18025–3906	27	−0.5 ± 0.15	6154	17 000	975–12 963	0.7	150	3.60×10^5	Q2
HD 335675	28	−0.9 ± 0.2	6082	16 000	7303–28 359	0.9	390	3.95×10^4	Q2
IRAS 19386+0155	29	−1.1 ± 0.14	6303	9600	4345–22 765	0.7	1000	6.00×10^3	Q2
IRAS 19475+3119	30	−0.24 ± 0.15	8216	6500	5955–7545	0.09	120	4.15×10^5	Q1
HR 7671	31	−1.6 ± 0.1	6985	3600	3449–3734	$<10^{-4}$	30	–	Q1
J052740.75–702842.0	LMC	−0.50	8283	5200	–	0.024	470	1.22×10^4	–
J045119.94–670604.8	LMC	−0.40	8280	5000	–	0.006	270	2.97×10^4	–
J052241.52–675750.2	LMC	−0.50	8284	5000	–	0.017	400	2.26×10^4	–
J050221.17–691317.2	LMC	−0.60	5250	4500	–	0.022	180	5.45×10^4	–
J051906.86–694153.9	LMC	−1.30	5613	3800	–	0.015	180	5.13×10^4	–

Notes. The quantities listed in the various columns are the following: 1: object name; 2: source ID (as reported in Kamath et al. 2022); 3 and 4: metallicity and effective temperatures, derived spectroscopically by Kamath et al. (2022); 5: luminosity derived in the present study for the Galactic sources; 6: luminosity from Kamath et al. (2022, see their Table 1), obtained in consideration of the upper and lower limits of the distances retrieved from Bailer-Jones et al. (2021); 7–9: optical depth at 10 μm, dust temperature and distance separating the central star from the inner border of the dusty region, found via SED fitting; 8: the quality flag (Q1 or Q2), based on the *Gaia* EDR3 renormalized unit weight error parameter, taken from Kamath et al. (2022). To ease the comparison with the results from Paper I, we report (in the 5 bottom lines) the non *s*-process enriched LMC sources studied in Paper I; for these sources, the metallicity and the effective temperature are from Kamath et al. (2015), while the luminosity and the dust properties are from Paper I.

This timescale is consistent with the distance of the dusty region derived from the SED fitting, if we assume that the dusty layer traveled with a velocity of ∼2 km s^{-1}.

3.2. Post-AGB stars that experienced HBB

Kamath et al. (2023) identified sources ID 21 and ID 27 as the progeny of massive AGB stars that experienced HBB. This conclusion is based on the surface chemical composition, which shows signs of nitrogen enrichment, whereas the [C/Fe] is slightly supersolar. The analysis of these sources offers the possibility to investigate dust production by massive AGBs, which was not possible in the study detailed in Paper I. This approach proves useful also to constrain the mass loss suffered during the late AGB phases by the stars that have experienced HBB. Unfortunately, they have both been flagged as Q2, thus, their distances are highly uncertain, as are their luminosities. As far as ID 21 is concerned, the post-HBB interpretation is consistent with the luminosity range given in Kamath et al. (2022); for what concerns ID 27, the luminosity range given by Kamath et al. (2022) is ∼1000−13 000 $L_\odot$, while the luminosities of post-HBB stars are expected to be above ∼17 000 $L_\odot$; however, given the Q2 flag, we believe that the luminosity of this source is underestimated.

Stars experiencing HBB descend from $M \geq 4\,M_\odot$ progenitors, which evolve on core masses above ∼0.8 $M_\odot$ (Ventura et al. 2013). As an example, we show in Fig. 6 the evolution of a 4 $M_\odot$ model star. These stars are characterized by a typical time variation of the luminosity (see left panel of Fig. 6), which increases during the first part of the AGB evolution, as the core mass increases, then diminishes during the final AGB phases, when HBB is gradually turned off, owing to the consumption of the convective envelope (Ventura et al. 2013; Karakas & Lattanzio 2014).

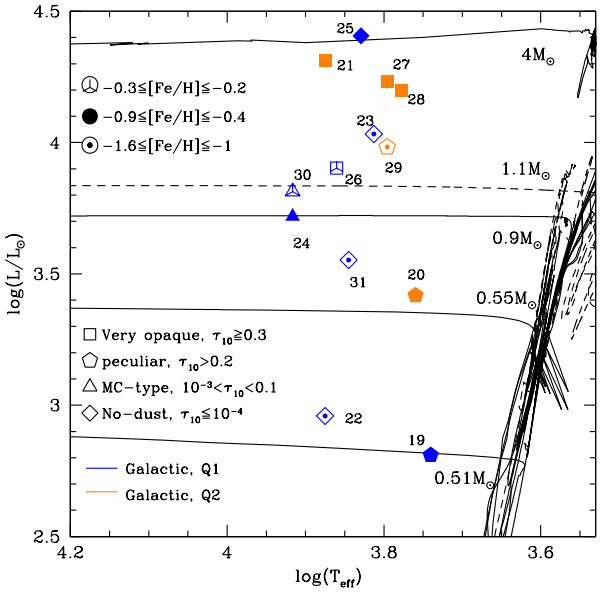

Fig. 3. Distribution of the oxygen-rich post-AGB stars studied here on the H-R diagram, according to the data reported in Table 1. The evolutionary tracks used for the interpretation of the individual objects are also shown, including the late AGB and the post-AGB phase; the tracks considered here have a metallicity of $Z = 0.004$ (solid lines) and $Z = Z_{\odot}$ (dashed line), and their mass at the beginning of the AGB phase is reported on the right side.

The mass-loss rate of this class of stars is rather uncertain: the use of different prescriptions leads to results that differ significantly in the values of the mass-loss rate experienced and in the way it changes along the AGB evolution. Overall, massive AGBs are efficient dust manufacturers. The dust formed is mostly under the form of silicates, with traces of alumina dust and solid iron (Ventura et al. 2012, 2014; Dell'Agli et al. 2014a). This approach holds in the case of solar or sub-solar chemical compositions only, because the scarcity of silicon and aluminium prevents significant dust formation during the evolution of metal-poor stars.

When the Blöcker (1995) treatment of mass loss is adopted, given the tight relationship between $\dot{M}$ and luminosity in the Blöcker (1995) formula, we find that the highest mass-loss rates take place in conjunction with the largest luminosity (compare the time variation of the luminosity and of the mass-loss rate in the left and right panel of Fig. 6, respectively). This will also be the phase when the dust production rate is highest, because the rate of mass loss affects directly the density of the wind (Ferrarotti & Gail 2006); thus affecting the number of gaseous molecules available to condense into dust.

To model ID 27, we considered a 4 $M_{\odot}$ model star of a metallicity $Z = 4\times10^{-3}$, which is consistent with the metallicity given by Kamath et al. (2022). As shown in the left panel of Fig. 6, this star reaches a peak luminosity ∼35 000 $L_{\odot}$, which decreases down to ∼22 000 $L_{\odot}$ during the final phases, preceding the contraction to the post-AGB evolution. Before the start of the contraction phase, the model star is characterized by an effective temperature of $T_{\rm eff} = 3400$ K, radius ∼500 $R_{\odot}$, period ∼1200 d, and mass 0.87 $M_{\odot}$.

In the right panel of Fig. 6, we can see that the largest mass-loss rate found when the Blöcker & Schöenberner (1991) treatment is used is $\dot{M} \sim 5 \times 10^{-5}\,M_{\odot}\,{\rm yr}^{-1}$, whereas during the final AGB phases it decreases to $\dot{M} \sim 10^{-5}\,M_{\odot}\,{\rm yr}^{-1}$. Dust formation modeling based on this mass-loss rate, combined with the values of luminosity, effective temperature, and mass given above, as well as with the surface chemistry of the star[2], leads to a TAGB optical depth $\tau_{10} = 0.4$. Using Eq. (4) of Paper I, which connects the current optical depth with the τ_{10} characterizing the star when the dust was last released, we find that the current optical depth should be $\tau_{10} \sim 5 \times 10^{-3}$. This is far lower than the value of τ_{10} derived for ID 27, reported in Table 1.

This result confirms recent findings by Marini et al. (2023) stating that the use of the mass-loss law by Blöcker (1995) during the final AGB phase hardly allows for the interpretation of the SED of dust-enshrouded AGB stars in the Galaxy, which are likely to have descended from massive AGBs undergoing HBB and are now evolving through the late AGB stages. On the other hand, Marini et al. (2023) found that use of the Vassiliadis & Wood (1993) treatment allows a much more satisfactory interpretation of the observations of these kind of sources. The application of the Vassiliadis & Wood (1993) recipe, when the values of luminosity, effective temperature, and period given above are considered, leads to TAGB optical depths $\tau_{10} \sim 5$, which corresponds to current optical depths that are consistent with the value found for ID 27 (see Table 1).

When using these enhanced mass-loss rates during the very final AGB phases, we find that the time interval between the tip of the AGB and the current epoch is ∼2000 yr. If we consider a later phase, when the effective temperature is 3500 K, the time interval is ∼400 yr. If we assume a velocity of ∼20 km s^{-1} we find that the distance traveled from dust corresponds to the value derived from SED fitting.

We note that this conclusion is independent of the way mass loss is described during the whole AGB evolution. The treatment of mass loss is definitively relevant for the duration of the whole AGB phase and it affects the number of TP experienced by the star; however, the conditions characterizing the very final AGB stages, after HBB is turned off, are practically independent of the previous AGB evolution, as they are mainly connected with the value of residual core mass when the final contraction begins.

The optical depths derived from these sources are consistent with the above discussion. For ID 27, we find $\tau_{10} = 0.7$, whereas for ID 21 we derive $\tau_{10} = 0.3$ from SED fitting. The difference between the two stars is mostly related to the lower metallicity of ID 21 than ID 27 and thereby to the lower quantities of silicon atoms available.

3.3. Dust-free stars

Sources ID 22 and 25 investigated by Kamath et al. (2022) show no infrared excess (see Fig. 2), which indicates that there is no dust in their surroundings – thus, no dust production occurred during the final part of the AGB phase. Indeed these sources populate the lower region of the plane shown in the left panel of Fig. 4, where we also find ID 23 and ID 31 whose SED exhibit small IR excess, corresponding to an optical depth of $\tau_{10} \leq 10^{-3}$. These sources are not reported in the right panel of the figure, as it was not possible to locate the dusty layer.

[2] The dust formed in the envelope of oxygen-rich stars is determined by the surface iron, silicon, and aluminium mass fractions; because the abundance of these elements does not change during the AGB phase, the initial chemical composition of the star is relevant for the amount of dust formed.

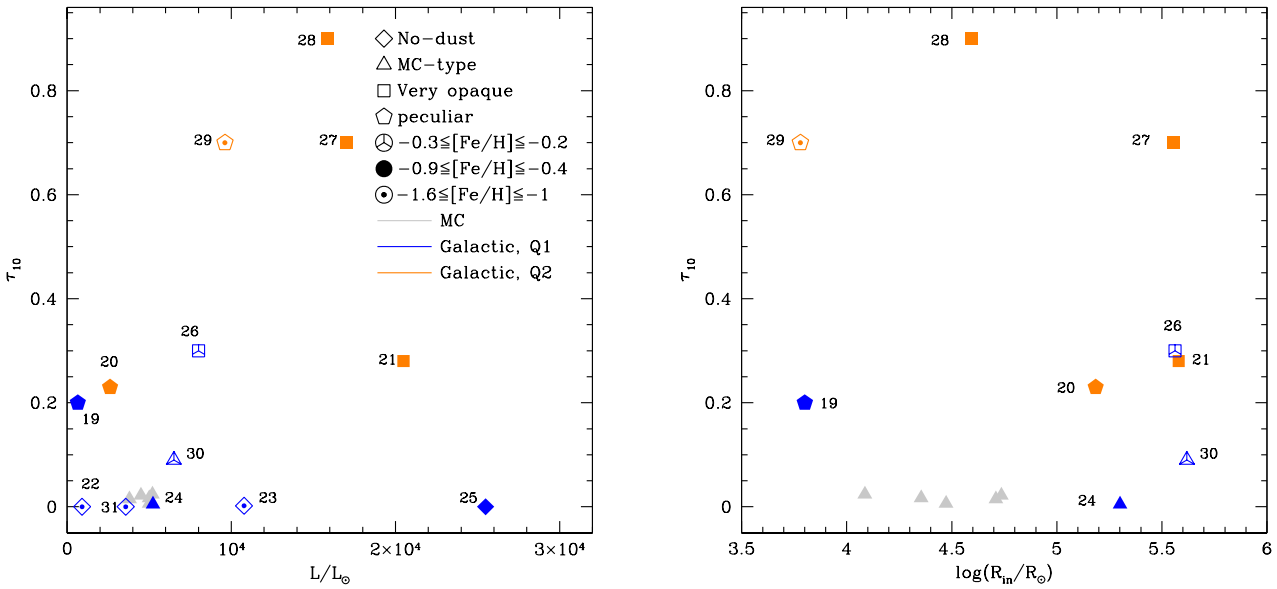

Fig. 4. Optical depths at the wavelength $\lambda = 10\,\mu$m (derived from SED fitting in Sect. 3) as a function of the luminosity of the star (left panel) and of the distance of the inner border of the dusty zone from the centre of the star (right panel). Color coding distinguishes the Galactic post-AGB stars flagged as Q1 (blue points) from those flagged as Q2 (orange). The gray triangles in the lower part of the plane refer to the LMC oxygen-rich post-AGB stars studied in Paper I.

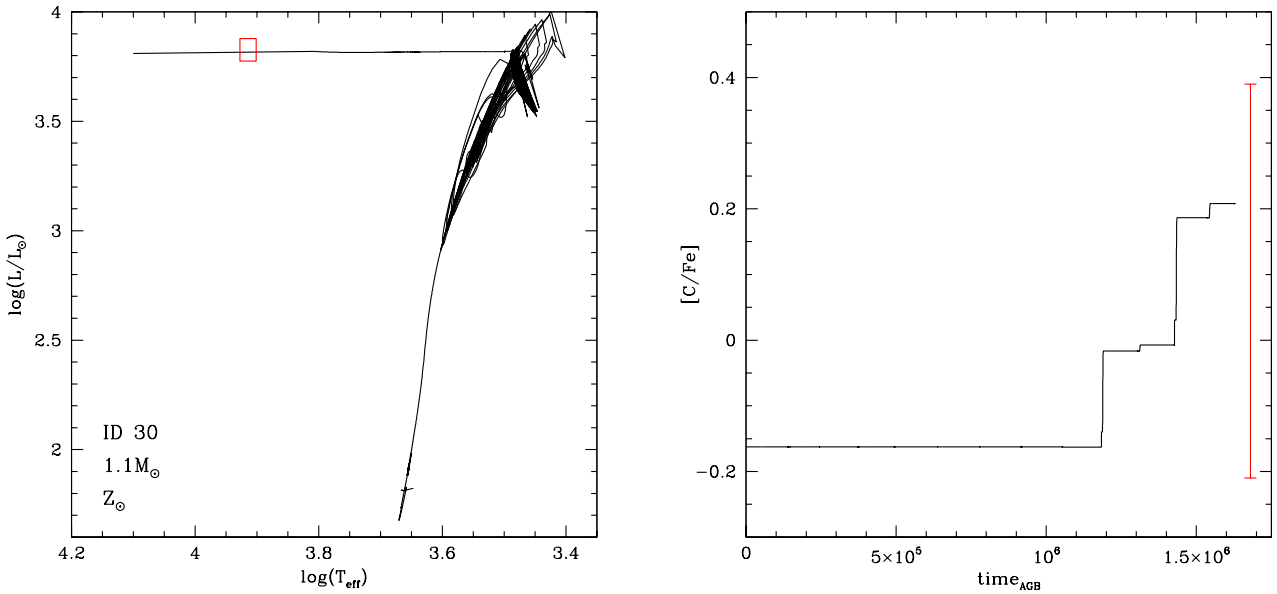

Fig. 5. Excursion of the evolutionary track of a 1.1 $M_\odot$ star of solar metallicity (left panel) and the variation of the surface carbon of the same 1.1 $M_\odot$ model star during the AGB phase. The red box on the left panel indicates the effective temperature and luminosity (with the corresponding error bars) given for ID 30 in Kamath et al. (2022), whereas the red vertical line in the right panel indicates the surface [C/Fe] of ID 30.

With regard to sources ID 22, 23, and 31, the lack of dust is due to the low metallicity (see Table 1), which prevents the formation of significant quantities of silicates and of alumina dust. This conclusion general and independent of the progenitor's mass and the current luminosity. More specifically, it stems from the fact that the formation of dust in the winds of oxygen-rich stars, unlike their carbon-rich counterparts, is extremely sensitive to the metallicity of the star (see van Loon 2000 for an observational point of view, while the theoretical predictions are discussed in Ferrarotti & Gail 2006; Ventura et al. 2014).

This explanation cannot be applied to ID 25, because the metallicity is [Fe/H] = −0.4. The luminosity is consistent with ∼4 $M_\odot$ progenitor, as discussed in Kamath et al. (2023). We note that this star is flagged as Q1, thus, the luminosity can be considered as fairly reliable. Stars of similar masses and metallicities experience HBB during the AGB evolution and are expected to produce significant quantities of silicates in their circumstellar envelopes ($\sim 2 \times 10^{-3}\,M_\odot$ during the entire AGB phase, see e.g., Ventura et al. 2014), which should be detectable at present. The signature of proton-capture nucleosynthesis is confirmed by the large N enhancement, with [N/Fe] slightly below unity, and the large fraction of sodium detected, namely, [Na/Fe] = +0.8 (Luck et al. 1990).

Among the results obtained in Paper I is the finding that bright stars are characterized by optical depths that are generally higher than their lower luminosity counterparts surrounded

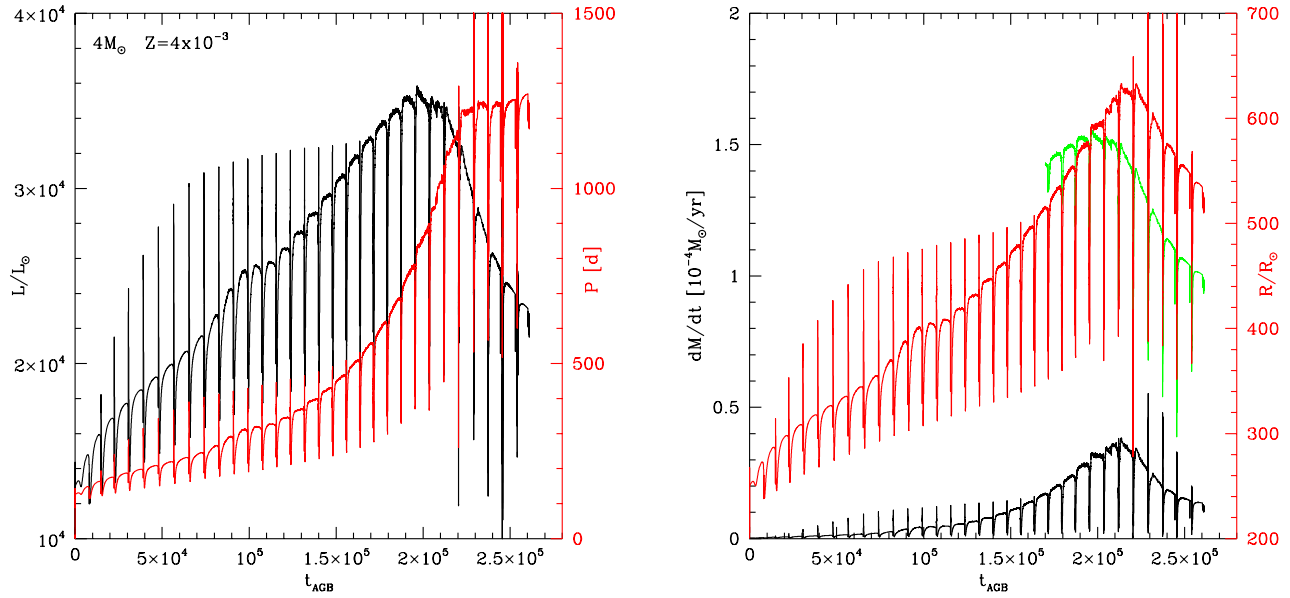

Fig. 6. Evolution of a 4 $M_\odot$ model star of metallicity $Z = 4 \times 10^{-3}$, in terms of the time variation of some physical quantities. Mass loss is modeled according to Blöcker & Schöenberner (1991). Times on the x-axis are zeroed at the beginning of the AGB phase. The left panel shows the variation of luminosity (black line, scale left y-axis) and pulsation period (red, scale on the right). The right panel shows the evolution of the mass-loss rate (black line) and of the stellar radius (red, scale on the right). The green line on the right panel shows the mass-loss rate that would be obtained during the super wind phase if the Vassiliadis & Wood (1993) prescription for mass loss was adopted.

by the same kind of dust. This is because the evolutionary times, particularly during the transition from the AGB to the post-AGB phase, are shorter; thus, the dust released is closer to the central object. All these factors render the post-AGB nature of ID 25 extremely unlikely. What is more likely is that the original classification by Luck et al. (1990), also considered by Van Winckel (1997), is valid; namely, this star is a supergiant and the surface N and Na have increased as a consequence of meridional currents active during the main sequence phase, triggered by the rotation of the star (Limongi & Chieffi 2018).

3.4. Low-luminosity stars as plausible AGB–manqué

Stars ID 19 and ID 20 are currently evolving at luminosities below the threshold required to start the TP phase (Kamath et al. 2022). Kamath et al. (2023) suggested that these objects descend from low-mass progenitors, which are evolving through the post-HB phase and have started the contraction to the blue after having evolved to the red. In this framework, it is during the latter phase that the dust observed presently was released, as no meaningful dust formation is expected for effective temperatures above 4000 K.

While on the evolutionary point of view this interpretation is consistent with results from stellar evolution modeling, the infrared excess exhibited by ID 19 and ID 20, which corresponds to $\tau_{10} = 0.2$ (see Fig. 4), is significantly higher than expected. Indeed the mass-loss rates obtained from stellar evolution modeling are slightly above $10^{-7}\ M_\odot\ \mathrm{yr}^{-1}$, which corresponds to optical depth below 0.05. The application of Eq. (4) from Paper I allows us to determine the current optical depth, $\tau_{10} \sim 0.01$, which is inconsistent with the values derived from the SED fitting.

ID 19 is a Q1 star, with a derived luminosity far below the threshold required to reach the TP phase. This suggests that it completed core helium burning, then evolved as a giant, before the envelope, of a few 0.01 $M_\odot$, was lost, and the evolutionary track moved to the blue side of the HR diagram. The contraction process must have been rather quick, owing to the low mass of the envelope, until the present-day effective temperature was reached. This is consistent with the results shown in the right panel of Fig. 2, where we notice that ID 19 is the star with the nearest dusty layer, below 10^4 solar radii.

ID 20 was flagged as Q2 by Kamath et al. (2022), which leaves some room for invoking a higher luminosity for this source. We believe it possible that the luminosity has been underestimated and that the true value is something around 4000 $L_\odot$. If this hypothesis proves correct, the star must have entered the AGB when the envelope mass was below 0.1 $M_\odot$ and then it was lost rapidly, likely as early as the first thermal pulse. This would be taking place in the wake of the scenario first proposed by Renzini (1989), which relies on the relatively long duration of the peak luminosity experienced by very low-stars.

An alternative explanation is based on the fact that the nitrogen abundance of ID 20 given in Kamath et al. (2022) is consistent with the results from HBB nucleosynthesis, when the upper values are considered. In this case ID 20 would descend from a massive AGB progenitor, which has experienced HBB. It is only an improved determination of the parallax that will allow for a better understanding of this object.

3.5. A few outliers

The sample of oxygen-rich stars with no s-process enrichment by Kamath et al. (2022) includes three sources for which a full understanding of the evolutionary and dusty properties can be barely reached. ID 26 is a peculiar object, as it is significantly enriched in nitrogen, despite the low luminosity. We note that this source is flagged as Q1 by Kamath et al. (2022), thus, the luminosity range given is reliable. Kamath et al. (2023) suggested that ID 26 had experienced deep mixing during the RGB

phase, which might explain the nitrogen and sodium enrichment measured.

On the other hand, this source is characterized by a large IR excess and the derived optical depth is $\tau_{10} = 0.3$, which is among the highest found in the present analysis. The occurrence of extra-mixing is not expected to affect the dust production during the final phases, which is relevant to determining the dust surrounding the star during the post-AGB. The dusty properties of this source suggest that the star descends from progenitors which experienced HBB. However, this result must be taken with some caution, given the claimed asymmetry in the dust distribution (Min et al. 2013), which might clash with the plain interpretation obtained here, based on the adoption of the DUSTY code in the isotropic modality.

In summary, while the surface chemistry and the dust properties of ID 26 are consistent with progenitors of mass above $\sim 3\,M_{\odot}$, which have experienced HBB and formed significant amounts of dust up until the end of the AGB phase. The luminosity is compatible with a low-mass progenitor.

The optical depth and the distance of the dusty layer from the star of ID 28 suggest that this source has descended from an intermediate mass progenitor. This interpretation could work if the upper limit for the metallicity reported in Table 1 is considered. We inserted this source among the outliers because the only derivation of the surface nitrogen by Şahin et al. (2011) appears to be inconsistent with the fact that ID 28 should have experienced HBB, which would lift the surface N by ∼1 dex.

ID 29 is one of the objects characterized by high optical depth, $\tau_{10} = 0.7$. Unfortunately, the luminosity of this source, flagged as Q2, is highly uncertain, with $4300\,L_{\odot} < L < 22\,800\,L_{\odot}$ (Kamath et al. 2022). Furthermore, the surface abundances of nitrogen and oxygen are not available. This prevents any identification of the progenitor and the interpretation of the IR excess. A further criticality related to this source is the possible presence of a disk, which would render futile the methodology used in the present analysis. Pereira et al. (2004) suggested, based on the morphology of the SED, that the star is surrounded by a dust disk. This conclusion is consistent with the results obtained by Goldman et al. (2017). Indeed, ID 29 appears to be the only source whose SED does not show the double-peak structure (see Fig. 1) that is otherwise typical of spherically symmetric sources. This is the reason for the poor agreement between the fit and the data, in particular in the region of the spectrum below $\lambda \sim 11\,\mu$m, regardless of the choice with regard to the percentage of crystalline silicate considered.

4. Discussion

The infrared excess characterizing post-AGB stars is related to the presence of dust in the surroundings of the stars that had been released during earlier epochs. On general grounds, the optical depth of the dusty region is determined by the rate of dust formation and by the current distance of the dusty region from the surface of the star; this distance is determined by the evolutionary time scale of the AGB to the post-AGB phase transition, as well as by the velocity with which the outflow moved away from the star after the dust was last released.

The situation for oxygen-rich stars emerging from this study is complex, as can be seen from Fig. 4, where it is clear that in this case, the luminosity (unlike the carbon stars investigated in Paper I) is not the only factor affecting the dust properties of post-AGB stars. Metal-poor oxygen-rich stars form little or no dust, independently of luminosity. If we restrict the attention on the sources with solar or sub-solar chemical composition, a rough correlation between luminosity and optical depth can be seen in the left panel of Fig. 4: the stars distribute on this plane along a diagonal band, covering the luminosity range $4000-18\,000\,L_{\odot}$ and the optical depths $5 \times 10^{-3} < \tau_{10} < 0.9$. ID 19 is off this trend, which might be connected to the fact that this star did not evolve through the AGB phase.

The optical depth of stars descending from massive AGBs that experienced HBB is generally higher than the low-mass counterparts of similar metallicity, owing to the larger rates of dust production experienced during the whole AGB lifetime, and particularly during the final AGB phases. However, an inspection of the right panel of Fig. 4 shows that the relationship between the distance of the dusty layer from the surface of the star and the luminosity is less straightforward than we previously found in Paper I for carbon stars in the MC.

We believe that the main reason for this is the intrinsic difference between the extinction properties of carbon dust and silicates, the mean opacities of carbonaceous dust being one order of magnitude higher than silicates, under the thermodynamic conditions when dust is expected to form (see Fig. 10 in Ferrarotti & Gail 2002). The scattering and absorption coefficients of carbon dust are extremely large, thus the formation of carbon dust, even in moderate quantities, favours a significant acceleration of the outflow: in these conditions, the current location of the dusty region is mainly determined by the time scale of the transition from the AGB to the post-AGB phase – thus, by the luminosity of the star.

In the case of the formation of silicates, it is not obvious that radiation pressure is able to overcome the gravitational pull of the central star and to accelerate the wind: this reflects into a higher heterogeneity in the outflow velocities of oxygen-rich stars with respect to carbon stars. As far as bright O-rich stars that have experienced HBB are considered, the luminosities around or above $2 \times 10^4\,L_{\odot}$ are sufficiently large so that the radiation pressure is strong enough to drive the wind. This is not as obvious in the low-luminosity ($L < 6000\,L_{\odot}$) domain of M-type stars. Indeed, in the low-luminosity region of the plane shown in the right panel of Fig. 4, populated by the progeny of low-mass stars that failed to reach the C-star stage, we note that the distance of the dusty region from the star is in fact correlated with the luminosity: the largest distance is found for ID 30, the brightest among these objects. A possible explanation for this behaviour is that by the combined analysis of the five oxygen-rich stars discussed in Paper I, as well as of ID 24 and ID 30, we are exploring the transition from winds scarcely affected by radiation pressure all the way to radiation-driven winds. This trend is reflected in the positive correlation between velocity and luminosity, which is the reason for the larger distances of the dusty regions in brighter stars.

We note in the right panel of Fig. 4 that the distance of the dusty regions of ID 30 is similar to those of the brighter, higher mass counterparts ID 21 and ID 27. We believe that even in this case, the explanation can be found in the different expansion velocities of the outflows which, in turn, are connected to the large differences between the dust production rates by low-mass and massive AGBs. In the case of the carbon stars investigated in Paper I, the difference in the mass-loss rates during the final AGB phases between the brighter stars and the low-luminosity C-stars was a factor of ∼3. In this case, we find that almost two orders of magnitude separate the mass-loss rate experienced by ID 27 ($\sim 10^{-4}\,M_{\odot}\,\mathrm{yr}^{-1}$) and ID 30 ($\sim 2 \times 10^{-6}\,M_{\odot}\,\mathrm{yr}^{-1}$). Since, for reasons of mass conservation, the velocity of the outflow is tightly connected with the mass-loss rate, thus the outflow velocity is significantly larger than in low-mass counterparts; this effect

counterbalances the differences in the evolutionary time scales when determining the location of the dusty region.

5. Conclusions

In this work, we study the properties of the dust surrounding oxygen-rich post-AGB stars to reconstruct the dust formation process during the late phases of the AGB evolution, which prove to be the most relevant in understanding the dust budget expected from low- and intermediate-mass stars. To this aim, we focus on oxygen-rich post-AGB sources observed in the Galaxy (Kamath et al. 2022), whose distances (and, hence, luminosities) can be inferred from the *Gaia* data release, for which the SED can be reconstructed with sufficient accuracy by the combined availability of results from optical and infrared photometry.

To reconstruct the evolutionary and dust formation history of these stars, we follow an approach based on the derivation of the main dust and stellar parameters via the SED fitting and on the interpretation of the results on the basis of stellar evolution and dust formation modeling of the AGB and post-AGB phases. This allowed us to identify: (a) sources descending from low-mass progenitors, which lose the external mantle before experiencing a number of TDU episodes sufficient to rise the surface *s*-process content and to reach the C-star stage; (b) the progeny of massive AGB stars that experienced HBB, which is further witnessed by the nitrogen enhancement derived from high resolution spectroscopy analysis; (c) stars with little or no IR excess, which we connect to the scarcity of dust in their surroundings; (d) faint sources, likely evolving through the post-HB phase, which failed to reach the AGB phase, owing to small mass of the envelope at the end of the core helium burning.

If we restrict our attention only to the stars belonging to the groups (a) and (b) mentioned above, we find that those of higher luminosity are surrounded by a more optically thick dusty region. This is consistent with the results from stellar evolution and dust formation modeling according to which the brighter stars of a given metallicity experience higher mass-loss and dust-production rates during the final AGB phases. Indeed, in the case of massive AGBs such a comparison between the observational evidence and the results from modeling allow us to draw information on the still largely unknown mass-loss mechanism experienced by these stars when evolving through the AGB phase, indicating that the rate of mass loss keeps above $\sim 10^{-4}\, M_{\odot}\, \mathrm{yr}^{-1}$ until the beginning of the transition from the AGB to the post-AGB phase.

An exception to this general behaviour is provided by a subset of metal poor stars, which have little or no dust in their surroundings, owing to the scarcity of silicon and aluminium in the surface regions. A further exception to this rule is the bright source ID 25, with a subsolar chemical composition and no dust, which we suggest is a red supergiant star.

The analysis of the distribution of the distances of the dusty regions from the central stars, derived from the SED fitting, offers an interesting opportunity to derive information regarding the dynamics of the winds of oxygen-rich stars, during the transition from the AGB to the post-AGB phase. In the low-mass domain, the distance of the dusty region is correlated to the luminosity, since brighter stars experience higher rates of dust formation than the lower luminosity counterparts of similar metallicity, thus, the outflow moves faster, owing to the higher radiation pressure acting on the dust grains in the circumstellar envelope. The analysis of the stars descending from massive AGB progenitors shows that the dusty regions are located at larger distances with respect to the ones found for the brightest low-mass stars. This is explained by the balance between the effects of the shorter transition time scales of higher luminosity stars and the greater dust production, which is reflected in faster outflows.

Acknowledgements. We thank the referee, Dr. Jacco Th. Van Loon, for his prompt, detailed and constructive revision of the manuscript. F.D.A. and P.V. acknowledge the support received from the PRIN INAF 2019 grant ObFu 1.05.01.85.14 ("Building up the halo: chemo-dynamical tagging in the age of large surveys", PI. S. Lucatello). D.K. acknowledges the support of the Australian Research Council (ARC) Discovery Early Career Research Award (DECRA) grant (DE190100813). This research was supported in part by the Australian Research Council Centre of Excellence for All Sky Astrophysics in 3 Dimensions (ASTRO 3D), through project number CE170100013. H.V.W. acknowledges support from the Research Council of the KU Leuven under grant number C14/17/082. E.M. acknowledges support from the INAF research project "LBT – Supporto Arizona Italia".

References

Belokurov, V., Penoyre, Z., Oh, S., et al. 2020, MNRAS, 496, 1922
Bailer-Jones, C. A. L., Rybizki, J., Fouesneau, M., Demleitner, M., & Andrae, R. 2021, AJ, 161, 147
Blöcker, T. 1995, A&A, 297, 727
Blöcker, T., & Schöenberner, D. 1991, A&A, 244, L43
Busso, M., Gallino, R., & Wasserburg, G. J. 1999, ARA&A, 37, 239
Cinquegrana, G. C., & Karakas, A. I. 2022, MNRAS, 510, 1557
Cristallo, S., Straniero, O., Piersanti, L., et al. 2015, ApJS, 219, 40
Dell'Agli, F., García-Hernández, D. A., Rossi, C., et al. 2014a, MNRAS, 441, 1115
Dell'Agli, F., Ventura, P., Garcia, Hernandez D., A., , et al. 2014b, MNRAS, 442, L38
Dell'Agli, F., Ventura, P., Schneider, R., et al. 2015a, MNRAS, 447, 2992
Dell'Agli, F., García-Hernández, D. A., Ventura, P., et al. 2015b, MNRAS, 454, 4235
Dell'Agli, F., Di Criscienzo, M., Boyer, M. L., et al. 2016, MNRAS, 460, 4230
Dell'Agli, F., Di Criscienzo, M., Ventura, P., et al. 2018, MNRAS, 479, 5035
Dell'Agli, F., Di Criscienzo, M., García-Hernández, D. A., et al. 2019, MNRAS, 482, 4733
Dell'Agli, F., Marini, E., D'Antona, F., et al. 2021, MNRAS, 502, L35
De Smedt, K., Van Winckel, H., Karakas, A. I., et al. 2012, A&A, 541, A67
Draine, B. T., & Lee, H. M. 1984, ApJ, 285, 89
Ferrarotti, A. S., & Gail, H.-P. 2002, A&A, 382, 256
Ferrarotti, A. S., & Gail, H.-P. 2006, A&A, 447, 553
García-Berro, E., Ritossa, C., & Iben, I. 1997, ApJ, 485, 765
García-Hernández, D. A., Manchado, A., Lambert, D. L., et al. 2009, ApJ, 705, L31
Ginolfi, M., Graziani, L., Schneider, R., et al. 2018, MNRAS, 473, 4538
Goldman, S. R., van Loon, J. T., Zijlstra, A. A., et al. 2017, MNRAS, 465, 403
Herwig, F. 2005, ARA&A, 43, 435
Iben, I., Jr. 1974, ARA&A, 12, 215
Jaeger, C., Mutschke, H., Begemann, B., Dorschner, J., & Henning, Th. 1994, A&A, 292, 641
Kamath, D. 2020, JApA, 41, 42
Kamath, D., & Van Winckel, H. 2022, Universe, 8, 233
Kamath, D., Wood, P. R., & Van Winckel, H. 2014, MNRAS, 439, 2211
Kamath, D., Wood, P. R., & Van Winckel, H. 2015, MNRAS, 454, 1468
Kamath, D., Van Winckel, H., Wood, P. R., et al. 2017, ApJ, 836, 15
Kamath, D., Van Winckel, H., Ventura, P., et al. 2022, ApJ, 927, L13
Kamath, D., Dell'Agli, F., Ventura, P., et al. 2023, MNRAS, 519, 2169
Karakas, A. I., & Lattanzio, J. C. 2014, PASA, 31, e030
Karakas, A. I., & Lugaro, M. 2016, ApJ, 825, 26
Karakas, A. I., Lugaro, M., Carlos, M., et al. 2018, MNRAS, 477, 421
Karakas, A. I., Cinquegrana, G., & Joyce, M. 2022, MNRAS, 509, 4430
Kobayashi, C., Karakas, A. I., & Lugaro, M. 2020, ApJ, 900, 179
Limongi, M., & Chieffi, A. 2018, ApJS, 237, 13
Lindegren, L., Klioner, S. A., Hernández, J., et al. 2021, A&A, 649, A2
Luck, R. E., Bond, H. E., & Lambert, D. L. 1990, ApJ, 357, 188
Marini, E., Dell'Agli, F., Kamath, D., et al. 2023, A&A, 670, A97
Min, M., Jeffers, S. V., Canovas, H., et al. 2013, A&A, 554, A15
Nanni, A., Bressan, A., Marigo, P., et al. 2013, MNRAS, 434, 2390
Nanni, A., Bressan, A., Marigo, P., et al. 2014, MNRAS, 438, 2328
Nanni, A., Marigo, P., Groenewegen, M. A. T., et al. 2016, MNRAS, 462, 1215
Nanni, A., Groenewegen, M. A. T., Aringer, B., et al. 2019, MNRAS, 487, 502
Nanni, A., Burgarella, D., Theulé, P., et al. 2020, A&A, 641, A168
Nenkova, M., Ivezic, Z., & Elitzur, M. 1999, PASP, 111, 1593

Penoyre, Z., Belokurov, V., Wyn Evans, N., Everall, A., & Koposov, S. E. 2020, MNRAS, 495, 321
Pereira, C. B., Lorenz-Martins, S., & Machado, M. 2004, A&A, 422, 637
Renzini, A. 1989, Planet. Nebulae, 131, 391
Romano, D., Karakas, A. I., Tosi, M., et al. 2010, A&A, 522, A32
Şahin, T., Lambert, D. L., Klochkova, V. G., et al. 2011, MNRAS, 410, 612
Sloan, G. C., Kraemer, K. E., Price, S. D., & Shipman, R. F. 2003, ApJS, 147, 379
Sloan, G. C., Matsuura, M., Zijlstra, A. A., et al. 2009, Science, 323, 353
Tosi, S., Dell'Agli, F., Kamath, D., et al. 2022, A&A, 668, A22
van Loon, J. T. 2000, A&A, 354, 125
Van Winckel, H. 1997, A&A, 319, 561
van Winckel, H. 2003, ARA&A, 41, 391
Vassiliadis, E., & Wood, P. R. 1993, ApJ, 413, 641
Ventura, P., & D'Antona, F. 2005a, A&A, 431, 279
Ventura, P., & D'Antona, F. 2005b, A&A, 439, 1075
Ventura, P., Zeppieri, A., Mazzitelli, I., & D'Antona, F. 1998, A&A, 334, 953
Ventura, P., Di Criscienzo, M., Schneider, R., et al. 2012, MNRAS, 420, 1442
Ventura, P., Di Criscienzo, M., Carini, R., & D'Antona, F. 2013, MNRAS, 431, 3642
Ventura, P., Dell'Agli, F., Schneider, R., et al. 2014, MNRAS, 439, 977
Ventura, P., Karakas, A., Dell'Agli, F., García-Hernández, D. A., & Guzman-Ramirez, L. 2018, MNRAS, 475, 2282
Ventura, P., Dell'Agli, F., Lugaro, M., et al. 2020, A&A, 641, A103
Ventura, P., Dell'Agli, F., Romano, D., et al. 2021, A&A, 655, A6
Vincenzo, F., Belfiore, F., Maiolino, R., et al. 2016, MNRAS, 458, 3466
Zhukovska, S., Gail, H.-P., & Trieloff, M. 2008, A&A, 479, 453